Advanced Modeling and Simulation in Engineering Sciences

RESEARCH ARTICLE Open Access

A multi-point constraint unfitted finite element method

Brubeck Lee Freeman*

*Correspondence:
freemanbl@cardiff.ac.uk

Cardiff University, Cardiff, UK

Abstract

In this work a multi-point constraint unfitted finite element method for the solution of the Poisson equation is presented. Key features of the approach are the strong enforcement of essential boundary, and interface conditions. This, along with the stability of the method, is achieved through the use of multi-point constraints that are applied to the so-called ghost nodes that lie outside of the physical domain. Another key benefit of the approach lies in the fact that, as the degrees of freedom associated with ghost nodes are constrained, they can be removed from the system of equations. This enables the method to capture both strong and weak discontinuities with no additional degrees of freedom. In addition, the method does not require penalty parameters and can capture discontinuities using only the standard finite element basis functions. Finally, numerical results show that the method converges optimally with mesh refinement and remains well conditioned.

Keywords: Unfitted finite element method, Cut element stability, Unfitted boundary conditions, Multi-point constraints, Unfitted interface, Extra dof free

Introduction

Over the last two decades unfitted finite element methods (UFEM), that allow the use of relatively simple background meshes, have proved to be useful tools for solving partial differential equations (PDE) on domains that may be highly complex and may evolve with time. Under the umbrella of unfitted finite element methods, a range of approaches and techniques have been developed including the generalised finite element method (GFEM) [1–11], extended finite element method (XFEM) [12–18] and cut finite element method (CutFEM) [19–25].

The generalised and extended finite element methods (GFEM and XFEM) are partition of unity methods [26, 27] that employ additional functions, or enrichments, to capture solution features, such as strong and weak discontinuities, internal to the elements. The enrichment functions are often chosen a priori based on the physics being simulated, though they may be calculated on the fly numerically, as seen in the global local GFEM [5]. In the work of Hansbo and Hansbo [19, 20], referred to as the phantom node method [28] or as the cut finite element method (CutFEM) [21], a different approach was taken. Instead of employing enrichment functions to capture discontinuities, their

approach can be described as replacing any element crossed by a discontinuity that splits the element into two parts, Ω_1 and Ω_2 with two overlapping elements T_1 and T_2. The new elements are each assigned to a part of the divided element and introduce additional nodes (termed phantom or ghost nodes), allowing the use of standard basis functions. This leads to a continuous solution in each element, u_1 and u_2, whilst their supposition allows for a discontinuous solution in the physical domain (defined as $u = u_1 \forall x \in \Omega_1 \wedge u = u_2 \forall x \in \Omega_2$). In each of these methods (GFEM, XFEM and CutFEM), the enrichments are associated with element nodes. An alternative approach is to associate the enrichments directly with the discontinuity itself, as seen in the discontinuity enriched (DEFEM) [29, 30] (see also the interface enriched method [31, 32]) and the element enriched finite element method (EFEM) [33–39].

Whilst UFEMs generally introduce additional degrees of freedom (dof) in order to capture solution features, approaches have been developed for UFEMs with the same number of unknowns as the standard finite element method (FEM). In EFEM models, a number of authors eliminate enriched degrees of freedom at the element level, often employing static condensation that increases the computational efficiency [33], at the cost of inter-element continuity. In addition, GFEM and XFEM models have been proposed that capture discontinuities with no additional degrees of freedom, namely condensed GFEM [8, 11], dof-gathering GFEM [7] and intrinsic and improved XFEMs [10, 14, 15, 40]. In these approaches, special enriched shape functions are employed that are constructed using least squares [8] or moving least squares [14, 15] over local patches of nodes. Bybordiani et al. [17] presented a multi-layered XFEM model for fracture propagation. In their approach, the discontinuities are enriched using independent layers, where each layer enriches a certain neighbourhood of cracked elements, defined using an active length scale parameter, λh. The size of the layers is bounded by limit cases of infinite and zero active lengths, recovering the XFEM and EFEM approaches respectively. Enriched degrees of freedom are eliminated using a condensation at the layer level.

A key challenge associated with UFEMs is the enforcement of essential boundary conditions on boundaries that are internal to the elements [41]. The most commonly used approaches employ a weak imposition of such conditions using the penalty method [42], Nitsche's method [19–21, 43, 44] and the Lagrange multiplier method [21, 45, 46]. The penalty method is easy to implement but is known for its propensity to degrade the condition number of the system; whilst the Lagrange multiplier method introduces additional unknowns that need to be defined in a suitable space to fulfil the inf–sup condition [45, 46]. Nitsche's method is a consistent penalty method, and as such does not degrade the condition number in the same manner as the penalty method [43]. An alternative approach to such methods, is to modify the element basis such that the boundary conditions are imposed exactly, as seen in the implicit boundary method [47]. In their model, van den Boom et al. [30] strongly enforced essential boundary conditions by constraining enriched nodes using multi-point constraints that are applied at the element level. In the cut-cell model presented by Pande et al. [48], exterior (ghost) nodes were constrained in a similar manner. The key difference being that in their work, these constraints replaced the governing equations for ghost nodes in the global system of equations.

An additional challenge for UFEMs lies in the fact that interfaces/boundaries may cross the underlying mesh arbitrarily. Whilst this is the key strength of such methods, the presence of degrees of freedom with small support in the physical domain can lead to stability issues. To counteract such issues, and to ensure so-called 'cut element stability', a number of approaches have been employed such as cell aggregation [49, 50], ghost penalties [21, 24, 51] and coupling constraints [44, 52]. The cell aggregation technique merges elements with small support to adjacent elements within the domain and is particularly suited to non-conforming finite element methods. The ghost penalty approach introduces a penalty on the jump in the normal derivative of the solution across element faces, weakly enforcing greater solution continuity. In the coupling constraints approach, degrees of freedom with small support are coupled to degrees of freedom in the interior using constraint equations derived from the finite element basis functions. An alternative to stabilising 'cut' elements is to avoid cutting the elements, as seen in the CutFEM model of Lozinski [23]. The shifted boundary method (SBM) introduced by Main and Scovazzi [53] (see also the shifted interface method (SIM) [54], and shifted fracture method (SFM) [55]), was introduced to avoid 'cut' elements whilst maintaining optimal convergence rates. In this approach, the boundary conditions are modified and shifted to a surrogate boundary that is formed from the nearest element edges/faces to the true boundary, before being imposed with Nitsche's method.

In the present work, the method proposed by Hansbo and Hansbo [19] is adopted for the unfitted finite element approximation. For the enforcement of essential boundary, and interface conditions, as well as cut element stability, multi-point constraints are employed. Constrained degrees of freedom are then removed, which leads to a global system of equations capable of capturing strong and weak discontinuities with no additional degrees of freedom.

The innovations of this work are (i) a new unfitted finite element model that, for the first time, strongly enforces essential boundary conditions, interface conditions and cut element stability using multi-point constraints, (ii) an approach to capturing strong and weak discontinuities in the solution with no additional degrees of freedom, avoiding the need for penalty parameters and using only the standard finite element basis functions and (iii) a numerical investigation of the performance of the model including mesh convergence and conditioning and its comparison to the model of Hansbo and Hansbo [19] and a standard FEM.

The remainder of this paper is organised as follows,

- "Problem formulation" presents the Poisson problem, including the case of a bi-material problem,
- "Unfitted finite element formulation" presents the unfitted finite element approximation and the multi-point constraint approach to enforcing essential boundary conditions, interface conditions and cut element stability,
- "Numerical examples" presents the application of the method to four example problems and its comparison to known analytical solutions,
- "Concluding remarks" presents some conclusions of the work.

Problem formulation

The present work is concerned with the solution of the Poisson problem that reads:

$$\begin{aligned} -\nabla \cdot (a\nabla u) &= f \quad in\ \Omega, \\ u &= g \quad on\ \Gamma_D, \\ \nabla_n u &= h \quad on\ \Gamma_N \end{aligned} \tag{1}$$

where $\Omega \in \mathbb{R}^2$ is the problem domain with boundary $\partial\Omega$, Γ_D and Γ_N are the parts of the boundary to which essential (Dirichlet) and Neumann boundary conditions are applied respectively and n is the outward facing unit normal to the boundary.

Equivalently, in the case of a bi-material problem, the problem reads:

$$\begin{aligned} -\sum_{i=1}^{2} \nabla \cdot (a_i \nabla u) &= f_i \quad in\ \Omega_1 \cup \Omega_2, \\ u &= g \quad on\ \Gamma_D, \\ \nabla_n u &= h \quad on\ \Gamma_N, \\ [\![u]\!] &= j \quad on\ \Gamma_i, \\ [\![a\nabla_n u]\!] &= k \quad on\ \Gamma_i \end{aligned} \tag{2}$$

where $[\![x]\!] = x_2|_{\Gamma_i} - x_1|_{\Gamma_i}$ is the jump operator, where $x_i = x|_{\Omega_i}$ is the restriction of x to Ω_i, and Γ_i is the material interface.

Unfitted finite element formulation

Unfitted finite element approximation

In the present work, the unfitted finite element method proposed by Hansbo and Hansbo [19] is employed. An example of this approach for a 1D problem with an interface is illustrated in Fig. 1. The coupling of the solutions in each overlapping element is determined by the interface conditions that are typically weakly enforced using Nitsche's method [21].

The finite element mesh is given by first defining a uniform background mesh, to which the physical domain is embedded. Following this, any elements that have zero intersection with the physical domain are removed, such that the computational mesh, T_h, is given as:

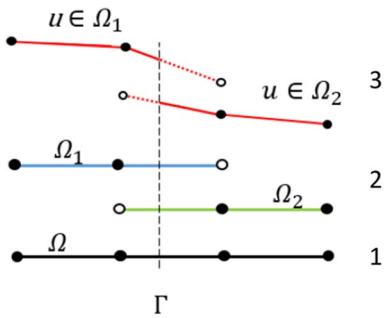

Fig. 1 (1) Original finite element mesh crossed by an interface, (2) Two overlapping finite element meshes with introduced ghost nodes (open circles), (3) Numerical solution where solid line indicates solution within the physical domain and the dashed line is the solution outside (after [51])

$$T_h = \left\{ T \in T_h^0 \middle| T \cap \Omega \neq \emptyset \right\} \tag{3}$$

where T denotes an element in the mesh and T_h^0 is the background mesh.

This process is illustrated in Fig. 2, where it can be seen that the computational domain, Ω_h, extends beyond the physical domain.

In the present work, the level set method is used to describe the domain boundary and material interfaces, and Q4 elements are used throughout. The boundary and interfaces are discretised using piecewise linear segments within each element.

Applying this approach to the Poisson problem, and integrating by parts over the computational domain, the weak form is given as:

Find $u \in H^1(\Omega)$, such that:

$$\int_\Omega \nabla v a \cdot \nabla u + \int_{\Gamma_N} v \cdot \nabla_n u = \int_\Omega v f + \int_{\Gamma_N} v h, \qquad \forall v \in H^1(\Omega) \tag{4}$$

where u is the solution vector and v are the test functions.

Employing the Galerkin weighted residual method for spatial discretisation gives:

$$K\overline{u} = F \tag{5}$$

where the primary variables are interpolated from the nodal value, i.e. $u = N\overline{u}$, where N is the vector of shape functions.

The global system matrix and right hand side vector are given as:

$$\begin{aligned} K &= \mathrm{A}_e \left(\int_{\Omega_e} \nabla N^T a \nabla N + \int_{\Gamma_{Ne}} N^T \nabla_n N \right) \\ F &= \mathrm{A}_e \left(\int_{\Omega_e} N^T f + \int_{\Gamma_{Ne}} N^T h \right) \end{aligned} \tag{6}$$

where A_e is the element assembly operator.

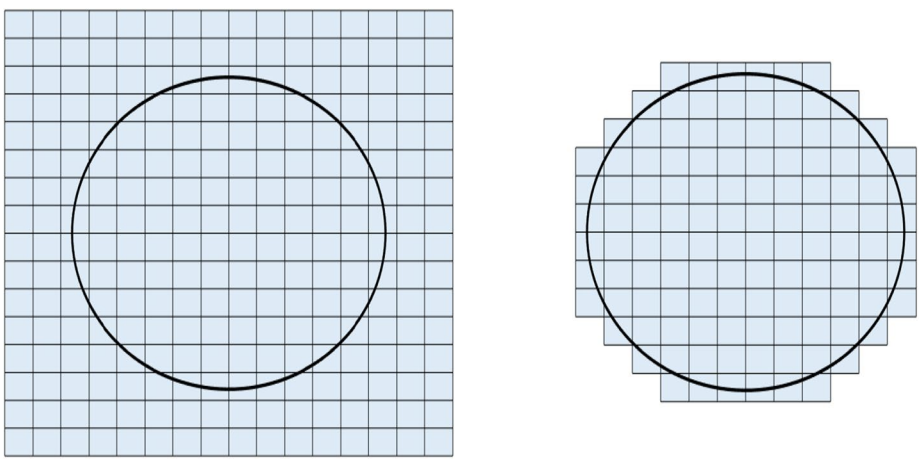

Fig. 2 (Left) A simple background mesh into which the physical domain is embedded, (right) the resulting computational mesh

An important aspect of Eq. (4) is that the divergence theorem is applied over the computational domain. This leads to a flux term associated with the boundary of the computational domain, $\partial\Omega_h$. This term does not appear in (4) as the degrees of freedom to which it applies, i.e. those that lie on $\partial\Omega_h$ are constrained and therefore are removed from the global system of equations. In addition, the integrals found in (4) are carried out over the physical domain that does not conform to the computational mesh. This implies that special integration rules are required for integrals over elements intersected by the problem boundary and/or interfaces (so-called cut elements). In the present work, volume integrals are carried out through the subdivision of cut elements into integration elements, to which the standard Gauss rule is applied; whilst surface integrals are taken over the piecewise linear approximation of the boundary and/or interfaces. A depiction of the subdivision can be seen in Fig. 3, where the shaded area indicates the physical domain.

Before describing the approach to enforcing constraints, the sets of nodes to which they are applied are first defined. Let $I_{gh} = \{i \in I | x_i \in \Omega_h \backslash \Omega\}$ be the set of global ghost nodes, where I is the global set of nodes and x_i are the coordinates of node i. The set of ghost nodes to which essential boundary conditions are applied is $I^D_{gh} \subset I_{gh} = \left\{i \in I_{gh} \middle| x_i \in T^D_h \wedge \left|x_i - x^P_i\right| < (1-\lambda)h\right\}$, in which, T^D_h is the set of elements that contains a part of the boundary to which essential boundary conditions are applied, x^P_i are the coordinates of the projection point for node i (to be introduced in following Section), h is the element size, λ is a user defined parameter and $||$ denotes the Euclidean distance. The last condition given in the set arises as the result of an assumption introduced to ensure boundedness of the solution, following the approach of Pande et al. [48]. The assumption is that any node at a distance $d \leq \lambda h$ from the boundary in fact lies on the boundary. As a result, the essential boundary condition is applied directly to such nodes, and multi-point constraints are not utilised for those points on the boundary. The set of ghost nodes to which interface conditions are applied can be defined similarly as $I^I_{gh} \subset I_{gh} = \left\{i \in I_{gh} \middle| x_i \in T^i_h \wedge \left|x_i - x^P_i\right| < (1-\lambda)h\right\}$, where T^i_h is the set of elements that contain a material interface. Finally, the set of nodes that are constrained to ensure cut element stability can be defined as $I^{CE}_{gh} = \left\{i \in I_{gh} \middle| i \notin I^D_{gh} \wedge i \notin I^I_{gh}\right\}$. In the present work, the parameter λ was set to 0.001 throughout.

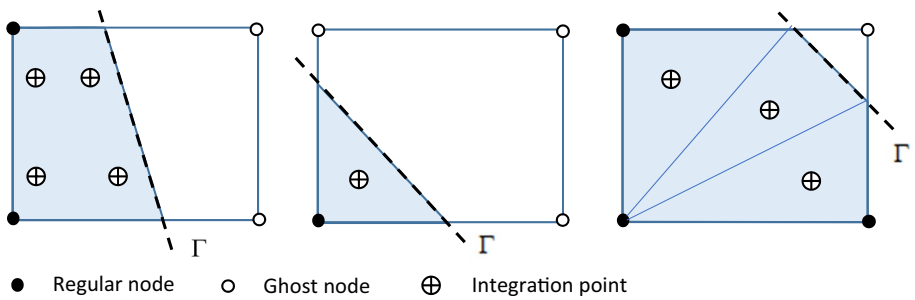

Fig. 3 A Q4 element crossed by a boundary showing the subdivision integration

Essential boundary conditions

The approach for enforcing essential boundary conditions follows the approach van den Boom et al. [30], and employs the interpolation of Pande et al. [48]. Following the approach of Pande et al. [48], a projection of the ghost nodes onto unique points on the physical boundary is employed. Four-noded bilinear elements (Q4 elements) are used for the present work, which implies that there may be either one, two or three ghost nodes. For a single ghost node, the projection is onto the centre of the boundary segment within that element, whereas for two ghost nodes the projection is onto the points of intersection of the boundary segment with the element edges. Finally, for three ghost nodes, a combination of the projections for a single and two ghost nodes is used. A depiction of the problem can be seen in Fig. 4, where Ω indicates the physical domain and the projection points are indicated by the crosses. Once the projection is established, the essential boundary condition is given as:

$$g(x,y) = N^T(x,y)u_e \tag{7}$$

where u_e is the vector of element nodal values.

In the work of Pande et al. [48], this condition replaces the equations for the ghost nodes in the system of equations. In the present work, the approach of van den Boom et al. [30] is followed and (7) is employed in the form of a multi-point constraint:

$$u_e^{gh} = -A^{-1}Bu_e^r + A^{-1}G \tag{8}$$

where u_e^{gh} and u_e^r are the vectors of degrees of freedom associated with ghost and regular nodes respectively, G is the vector of prescribed values and A and B are the matrices of shape functions of ghost and regular degrees of freedom respectively, evaluated at the projection points. Using (8), the element matrix and right-hand side vector are modified as follows:

$$\begin{aligned} \hat{K}_e &= T_I' K_e T_D \\ \hat{F}_e &= T_I'(F_e - K_e G_T) \end{aligned} \tag{9}$$

where T_D is the transformation matrix that contains the contributions of the regular degrees of freedom to the ghost nodes, and G_T is comprises the prescribed values.

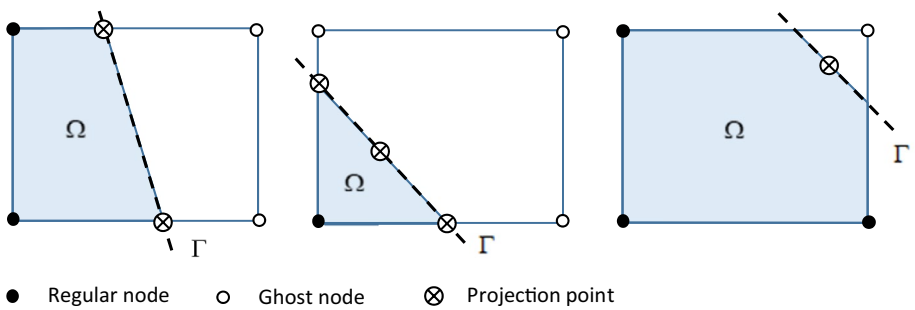

Fig. 4 A Q4 element crossed by a boundary showing the three possible cases

Finally, $T_I = \delta_{ij} \forall i \in n_r \wedge T_I = 0 \forall i \in n_{gh}$, where n_r is the set of local regular nodes and n_{gh} is the set of local ghost nodes, is used to eliminate the ghost nodes from the system of equations.

In the reduced matrices described in (9), the boundary conditions are strongly enforced.

To illustrate the procedure, consider a Q4 element crossed by a boundary such that there are three ghost nodes (see Fig. 4), subject to essential boundary conditions. In this case Eq. (8) becomes:

$$\begin{aligned}\begin{bmatrix} u_2 \\ u_3 \\ u_4 \end{bmatrix} = &- \begin{bmatrix} N_2(x_1,y_1) & N_3(x_1,y_1) & N_4(x_1,y_1) \\ N_2(x_2,y_2) & N_3(x_2,y_2) & N_4(x_2,y_2) \\ N_2(x_3,y_3) & N_3(x_3,y_3) & N_4(x_3,y_3) \end{bmatrix}^{-1} \begin{bmatrix} N_1(x_1,y_1) \\ N_1(x_2,y_2) \\ N_1(x_3,y_3) \end{bmatrix} [u_1] \\ &+ \begin{bmatrix} N_2(x_1,y_1) & N_3(x_1,y_1) & N_4(x_1,y_1) \\ N_2(x_2,y_2) & N_3(x_2,y_2) & N_4(x_2,y_2) \\ N_2(x_3,y_3) & N_3(x_3,y_3) & N_4(x_3,y_3) \end{bmatrix}^{-1} \begin{bmatrix} g_{x1} \\ g_{x2} \\ g_{x3} \end{bmatrix}\end{aligned} \tag{10}$$

where the coordinates correspond to the projection points. The non-zero terms of the transformation matrix become:

$$\begin{aligned} T_{D11} &= 1 \\ T_{D21} &= A_{11}^{-1} B_1 + A_{12}^{-1} B_2 + A_{13}^{-1} B_3 \\ T_{D31} &= A_{21}^{-1} B_1 + A_{22}^{-1} B_2 + A_{23}^{-1} B_3 \\ T_{D41} &= A_{31}^{-1} B_1 + A_{32}^{-1} B_2 + A_{33}^{-1} B_3 \end{aligned} \tag{11}$$

whilst the terms of the vector of prescribed values read:

$$\begin{aligned} G_{T2} &= A_{11}^{-1} g_{x1} + A_{12}^{-1} g_{x2} + A_{13}^{-1} g_{x3} \\ G_{T3} &= A_{21}^{-1} g_{x1} + A_{22}^{-1} g_{x2} + A_{23}^{-1} g_{x3} \\ G_{T4} &= A_{31}^{-1} g_{x1} + A_{32}^{-1} g_{x2} + A_{33}^{-1} g_{x3} \end{aligned} \tag{12}$$

Interface conditions

The approach to enforcing interface conditions follows the same procedure as that for enforcing essential boundary conditions. The key difference is that now jump conditions are enforced, in both the solution itself and in the solution gradient. In addition, in this case the number of ghost nodes is always equal to the number of nodes of the element, irrespective of how the discontinuity crosses the element. In the present case as Q4 elements are employed, there are four ghost nodes. As before, the approach begins with a projection of the ghost nodes onto the physical interface. The projection points are at the points of intersection between the boundary segment and the element edges. A depiction of this can be seen in Fig. 5, where Ω_1 and Ω_2 indicate the physical domain on the positive and negative sides of the interface respectively and where it is noted that at each projection point, both interface conditions are evaluated. Once the projection is established, the interface conditions that depend upon the problem considered are given as:

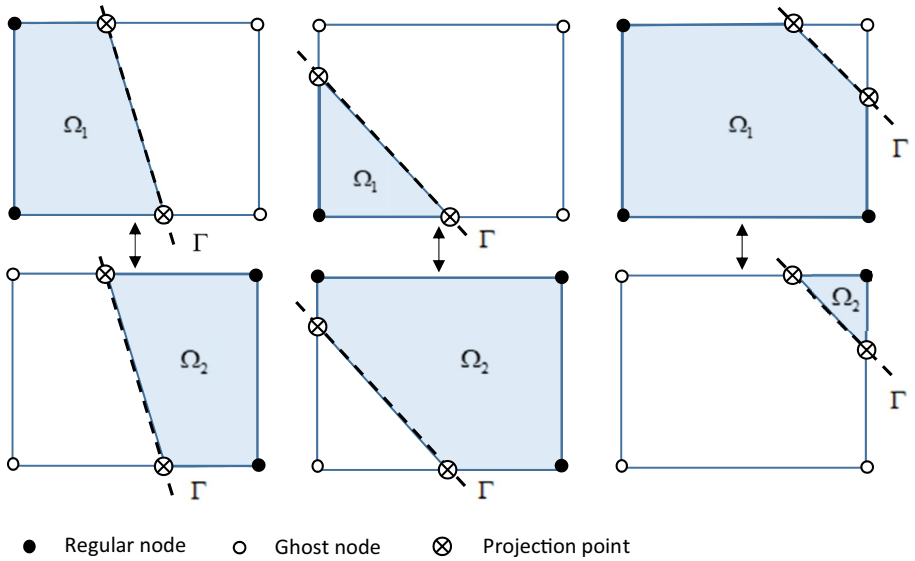

Fig. 5 A Q4 element crossed by an interface, showing the three possible cases, where the arrows indicate coupled overlapping elements

$$\begin{aligned} j(x,y) &= \left[\left[N^T(x,y)u_e\right]\right] \\ h(x,y) &= \left[\left[\nabla_n N^T(x,y)u_e\right]\right] \end{aligned} \tag{13}$$

The first equation in (13) enforces the condition on the jump in the solution, whilst the second enforces the condition on the jump in the solution gradient. Using (13), the same procedure as before is followed that leads to reduced matrices, in which the interface conditions are strongly enforced. In this case, the matrices A and B (see Eq. (8)) are of shape functions and shape function derivatives of the ghost and regular nodes respectively, evaluated at the projection points, and G (Eq. (8)) is the vector of the prescribed jumps in both the solution and in the solution gradient.

To illustrate the difference to enforcing essential boundary conditions, consider a Q4 element crossed by a boundary such that there are three ghost nodes associated with Ω_1, and one ghost node associated with Ω_2 (see Fig. 5), subject to the interface conditions described in (13). In this case, Eq. (8) becomes:

$$\begin{bmatrix} u_2^1 \\ u_3^1 \\ u_4^1 \\ u_1^2 \end{bmatrix} = -A^{-1}B \begin{bmatrix} u_1^1 \\ u_2^2 \\ u_3^2 \\ u_4^2 \end{bmatrix} + A^{-1} \begin{bmatrix} j_{x1} \\ h_{x1} \\ j_{x2} \\ h_{x2} \end{bmatrix} \tag{14}$$

where the superscript denotes the domain (i.e. $u_1^i \in \Omega_i$) and the matrices are given as:

$$A = \begin{bmatrix} N_2^1(x_1,y_1) & N_3^1(x_1,y_1) & N_4^1(x_1,y_1) & -N_1^2(x_1,y_1) \\ \nabla_n N_2^1(x_1,y_1) & \nabla_n N_3^1(x_1,y_1) & \nabla_n N_4^1(x_1,y_1) & -\nabla_n N_1^2(x_1,y_1) \\ N_2^1(x_2,y_2) & N_3^1(x_2,y_2) & N_4^1(x_2,y_2) & -N_1^2(x_2,y_2) \\ \nabla_n N_2^1(x_2,y_2) & \nabla_n N_3^1(x_2,y_2) & \nabla_n N_4^1(x_2,y_2) & -\nabla_n N_1^2(x_2,y_2) \end{bmatrix} \tag{15}$$

$$B = \begin{bmatrix} N_1^1(x_1,y_1) & -N_2^2(x_1,y_1) & -N_3^2(x_1,y_1) & -N_4^2(x_1,y_1) \\ \nabla_n N_1^1(x_1,y_1) & -\nabla_n N_2^2(x_1,y_1) & -\nabla_n N_3^2(x_1,y_1) & -\nabla_n N_4^2(x_1,y_1) \\ N_1^1(x_2,y_2) & -N_2^2(x_2,y_2) & -N_3^2(x_2,y_2) & -N_4^2(x_2,y_2) \\ \nabla_n N_1^1(x_2,y_2) & -\nabla_n N_2^2(x_2,y_2) & -\nabla_n N_3^2(x_2,y_2) & -\nabla_n N_4^2(x_2,y_2) \end{bmatrix} \tag{16}$$

The terms of (14) can then be used to define the transformation matrix and vector of prescribed values as before. The only difference being their dimension is now doubled as the transformation is now applied to the two overlapping elements. The resulting reduced matrices have the same dimension as a standard element.

Cut element stability

Stability issues associated with cut elements arise from the fact that some of the degrees of freedom have very small support in the physical domain. This can lead to severe ill-conditioning of the system of equations and can have a detrimental affect on convergence [50]. In Rüberg et al. [44] (see also Höllig et al. [51]); stability was ensured through coupling degrees of freedom with small support to degrees of freedom within the interior of the domain using constraints.

In the present work, all degrees of freedom that lie outside of the physical domain (ghost degrees of freedom) are constrained. The ghost degrees of freedom are then removed from the system of equations. Before describing the approach, it is emphasised that this type of constraint is only applied to ghost nodes that are not already constrained by either essential boundary, or interface conditions.

The first step in the approach is, for all eligible ghost nodes, the nearest element, T_{nr}, that lies entirely within the physical domain is found. Following this, the constraint equation is evaluated as:

$$u^{gh}(x,y) = N^T(x,y)u_e - fd^2 \tag{17}$$

where the vector of shape functions and nodal values are those associated with T_{nr} and d is the distance to the centre of T_{nr}, from the centre of the nearest element to which u^{gh} belongs. A key thing to note about (17) is the fact that the shape functions are evaluated at the ghost node location that lies outside of the reference element. In the present work, the shape functions that are used in (17) use global coordinates, and as such their evaluation outside of the reference element is straightforward. The last term in (17) is included in order to account for the effect of the source term on the extrapolation.

Using (17), we can follow a similar procedure to before that leads to reduced matrices within which, the constraints are strongly enforced. A key difference is the fact that constraints of the type described in (17) lead to a larger support size and as such, the constraints are applied in the system assembly rather than at the element level.

To illustrate the procedure consider the two elements in Fig. 6, the first of which lies completely inside the physical domain, whilst the second is crossed by the domain boundary. In this case the nearest element interior to the domain has been identified and will be used to constrain the degree of freedom associated with the ghost node,gh.

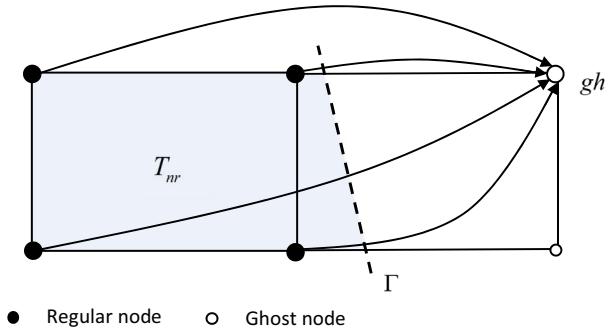

Fig. 6 Illustration of cut element stabilisation, the degrees of freedom at *gh* are coupled to those associated with the nearest element interior to the domain, T_{nr}, as indicated by the arrows

Numerical examples

In this section, example problems are presented in order to demonstrate the performance of the model. The example problems concern the three cases of unfitted elements, namely, an unfitted Neumann boundary condition, an unfitted interface (considered with both a weak and a strong discontinuity) and two cases with unfitted essential boundary conditions on a curved boundary. In each case, the numerical solutions are compared to known analytical solutions and the mesh convergence and conditioning of the system are investigated. In addition, in the second example the predictions of the proposed model are compared to those of Hansbo and Hansbo [19], as well as those of a standard FEM.

Heat conduction with unfitted Neumann boundary condition

The first example concerns heat conduction in a rod with a source term subject to fixed temperature on the left hand side of the specimen and an unfitted Neumann boundary condition on the right hand side of the specimen. The equation describing this example reads:

$$\begin{aligned} -\Delta u &= 10, \\ u(0) &= 0, \\ \nabla_n u(0.95) &= 0 \end{aligned} \tag{18}$$

where the physical domain is $\Omega = (0, 0.95)$ and the background mesh domain is $\Omega_m = (0, 1.1)$. The analytical solution is given by:

$$u(x) = -5x^2 + 9.5x \tag{19}$$

An example of one of the meshes used in the analysis that shows the boundary marked with a black line, can be seen in Fig. 7.

The performance of the model with mesh refinement can be seen in Fig. 8, that shows the L_2-norm of the error, $e = \|u - u_{ex}\|_{L_2}$ [48], where u_{ex} is the exact solution, along with the 2-norm condition number. From the figure, it can be seen that the method converges optimally (i.e. of the order h^2) and that the system is well conditioned (i.e. of the order h^{-2}).

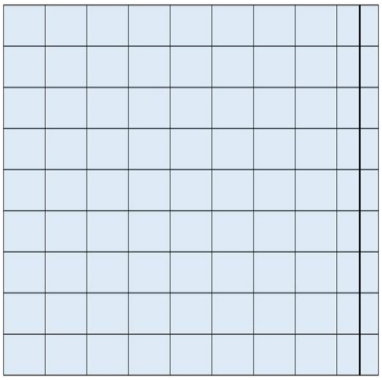

Fig. 7 Finite element mesh used in the analysis and unfitted boundary

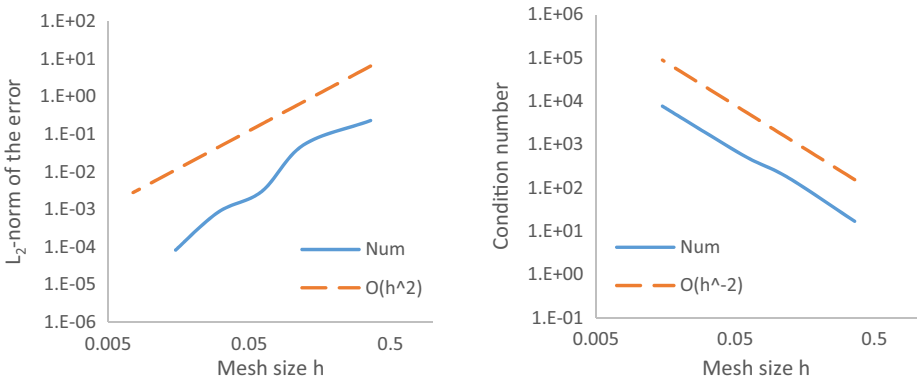

Fig. 8 Plot of the L_2-norm of the error and 2-norm condition number

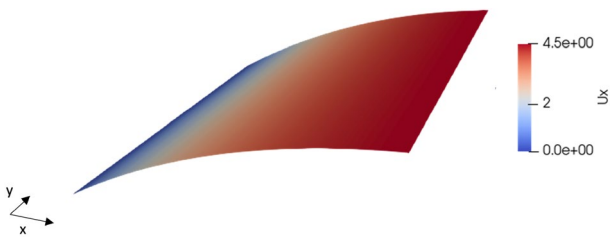

Fig. 9 Elevation of the numerical solution

The solution for the finest mesh can be seen in Fig. 9.

In addition to investigating the error and condition number under mesh refinement, this example was also used to investigate the effect of the boundary location with respect to the element edges (see Fig. 10). To this end, the mesh with $h = 0.061$ was employed and the condition number calculated for a range of boundary locations. The results of this investigation can be seen in Fig. 10, which shows that the system remains well conditioned when cut element stabilisation is employed. By contrast, when stabilisation is not employed the condition number deteriorates at a rate of the order d^{-1}, as reported in [44].

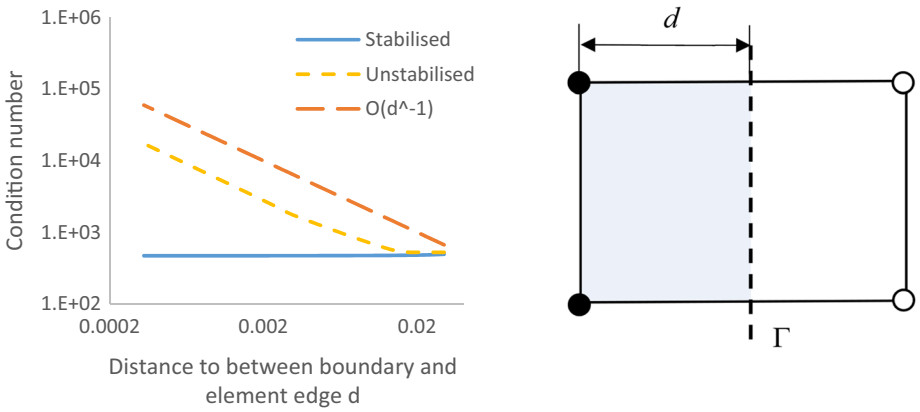

Fig. 10 Plot of the 2-norm condition number for different boundary locations and schematic showing unfitted boundary and distance to element edge *d*

This example indicates that the method performs well for unfitted Neumann boundary conditions, and for arbitrary intersections between the boundary and underlying mesh.

Poisson interface problem with unfitted weak and strong discontinuity

The second example considers the solution to the Poisson interface problem as presented in Hansbo and Hansbo [19], subject to essential boundary conditions:

$$\begin{aligned} &-\sum_{i=1}^{2} \nabla \cdot (a_i \nabla u) = 1, \\ &[\![u(1/2)]\!] = 0, \\ &[\![a\nabla u(1/2)]\!] = 0, \\ &u(0) = 0, \\ &u(1) = 0 \end{aligned} \tag{20}$$

where the physical and background mesh domains are $\Omega = \Omega_m = (0, 1)$. The interface is unfitted and located at $x = 1/2$, and $a_1 = 1/2$ and $a_2 = 3$. The analytical solution if given by:

$$\begin{aligned} u_1(x) &= \frac{(3a_1 + a_2)x}{4a_1^2 + 4a_1a_2} - \frac{x^2}{2a_1}, \\ u_2(x) &= \frac{a_2 - a_1 + (3a_1 + a_2)x}{4a_2^2 + 4a_1a_2} - \frac{x^2}{2a_2} \end{aligned} \tag{21}$$

An example of one of the meshes used in the analysis that shows the interface marked with a black line can be seen in Fig. 11.

The results of the convergence test can be seen in Fig. 12, whilst the solution for the finest mesh can be seen in Fig. 13. From the figure, we can again see that the method converges optimally and remains well conditioned.

A comparison between the results of the present method, the method of Hansbo and Hansbo [19] and the standard FEM (taken from [19]), both with a fitted and unfitted mesh, can be seen in Fig. 14. It can be seen from the figure that the performance of the proposed approach is comparable to both that of Hansbo and Hansbo [19] and that of a standard

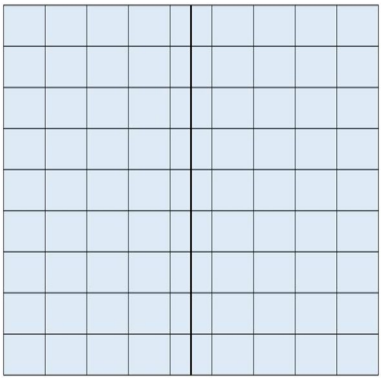

Fig. 11 Finite element mesh used in the analysis and unfitted interface

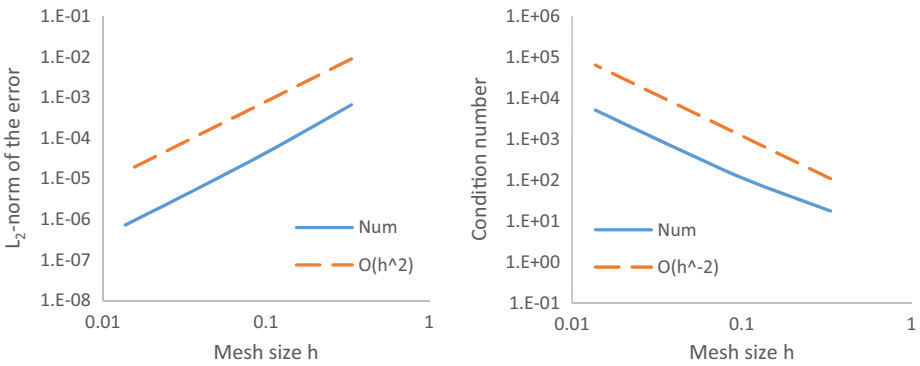

Fig. 12 Plot of the L_2-norm of the error and 2-norm condition number

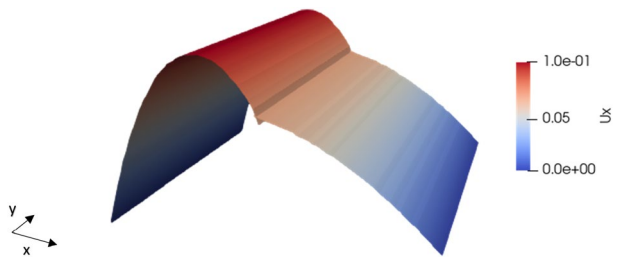

Fig. 13 Elevation of the numerical solution

FEM when an interface fitted mesh is employed. The results show that the standard FEM with an unfitted interface does not show optimal convergence, and as such finer meshes would be required to achieve the same level of accuracy.

In addition to simulating the problem as presented in Hansbo and Hansbo [19], a modified form with a strong discontinuity is also considered. In this case the interface and boundary conditions become:

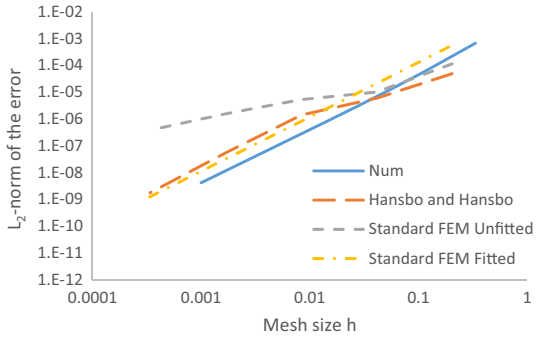

Fig. 14 Comparison of the convergence of present approach to Hansbo and Hansbo [19] and the standard FEM with a fitted and unfitted mesh

$$\begin{aligned} &[\![u(1/2)]\!] = 0.02, \\ &[\![a\nabla u(1/2)]\!] = 0, \\ &u(0) = 0, \\ &u(1) = -0.02 \end{aligned} \tag{22}$$

Whilst the analytical solution reads:

$$\begin{aligned} u_1(x) &= \frac{(3a_1 + a_2)x}{4a_1^2 + 4a_1a_2} - \frac{x^2}{2a_1}, \\ u_2(x) &= \frac{a_2 - a_1 + (3a_1 + a_2)x}{4a_2^2 + 4a_1a_2} - \frac{x^2}{2a_2} - 0.02 \end{aligned} \tag{23}$$

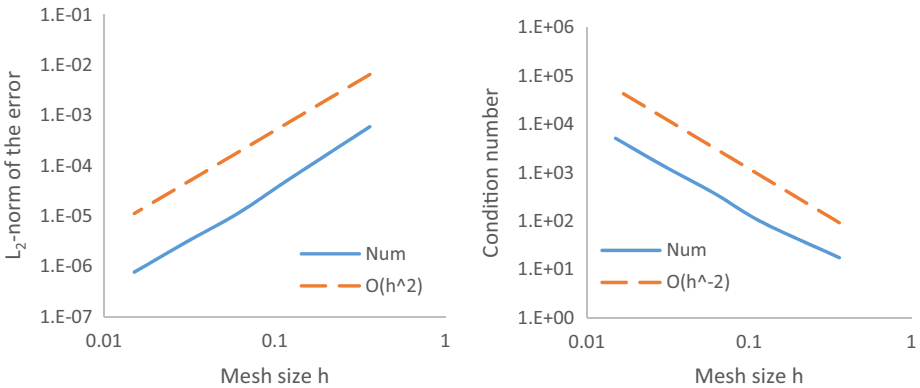

Fig. 15 Plot of the L_2-norm of the error and 2-norm condition number

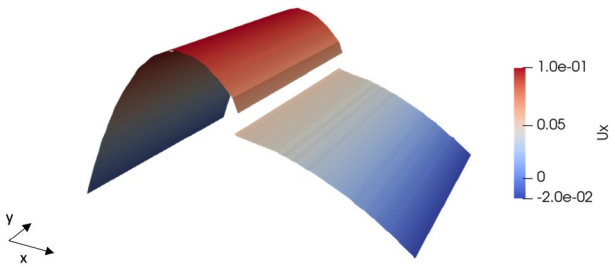

Fig. 16 Elevation of the numerical solution

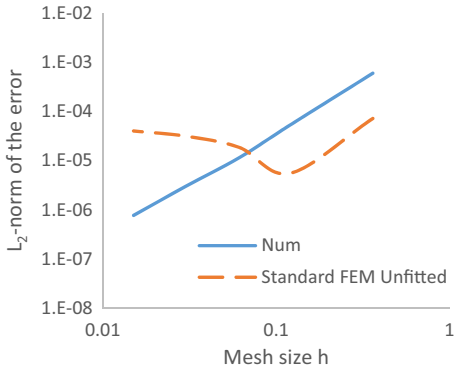

Fig. 17 Plot of the L_2-norm of the error and comparison with the standard FEM with an unfitted mesh

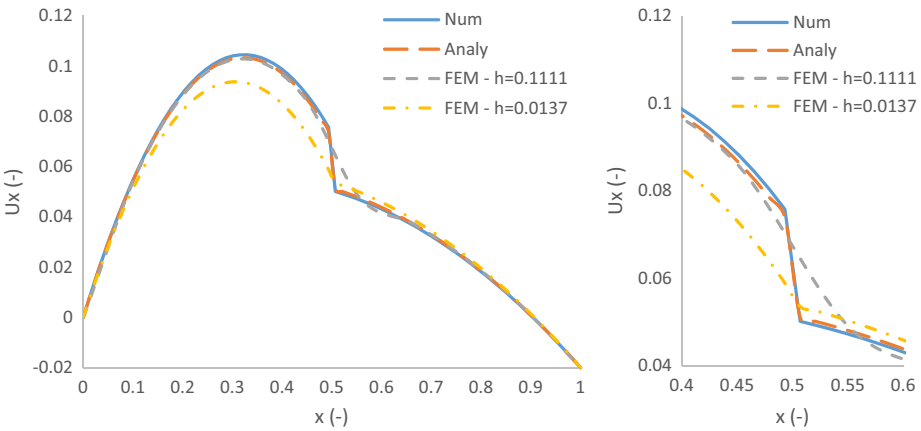

Fig. 18 Comparison of the numerical solution to the analytical solution and predictions from a standard FEM (left) Full solution profile and (right) close up of solution profile near the interface

The results of the convergence test can be seen in Fig. 15, whilst the solution for the finest mesh can be seen in Fig. 16. From the figure, it can again be seen that the method converges optimally and remains well conditioned.

A comparison of the convergence of the approach as compared to the standard FEM with an unfitted mesh can be seen in Fig. 17. It can be seen from the figure that the standard FEM does not converge optimally, and that the error actually increases with further mesh refinement. A comparison between the predicted solutions and the analytical solution can be seen in Fig. 18. From the figure it can be seen that the proposed model predictions are coincident with the analytical solution, whilst the standard FEM is unable to capture the jump in the solution. It is noted that in this case the standard FEM with an interface fitted mesh would also suffer from sub-optimal convergence due to jump in the solution that would require the use of interface elements to be captured.

This example indicates that the method performs well for unfitted interface problems with both weak and strong discontinuities and is comparable with the performance of the model of Hansbo and Hansbo [19].

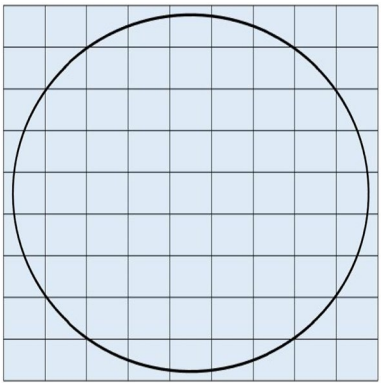

Fig. 19 Finite element mesh used in the analysis and unfitted boundary

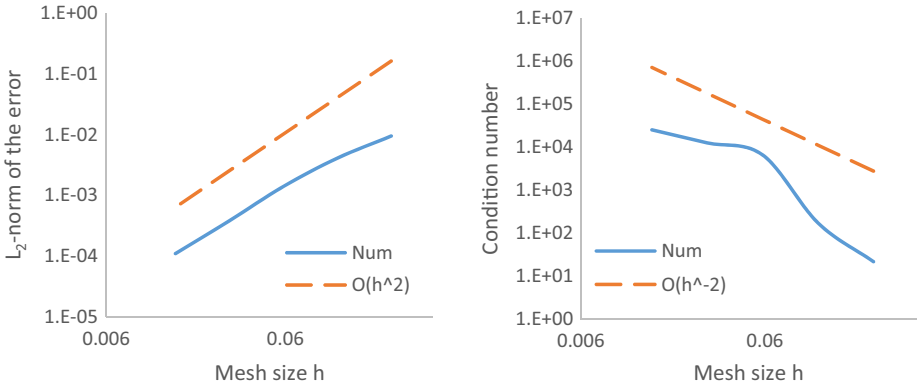

Fig. 20 Plot of the L_2-norm of the error and 2-norm condition number

Poisson problem on circular domain with unfitted essential boundary

The third example considers the solution of the Poisson equation in circular domain subject to unfitted essential boundary conditions [48]:

$$\begin{aligned} -\Delta u &= 1, \\ u(0.95, \theta) &= 0.1 \end{aligned} \tag{24}$$

where the physical domain is defined $\Omega = (0, 0.95) \times (0, 2\pi)$ and the background mesh domain is $\Omega_m = (-1.05, 1.05) \times (-1.05, 1.05)$. The analytical solution is given by:

$$u(r, \theta) = \frac{\left(0.95^2 - r^2\right)}{4} + 0.1 \tag{25}$$

It can be noted that whilst this is a radial problem, the numerical solution was carried out using Cartesian coordinates. In addition, the circular boundary of the physical domain is approximated using piecewise linear segments within each element.

An example of one of the meshes used in the analysis that shows the boundary marked with a black line, can be seen in Fig. 19.

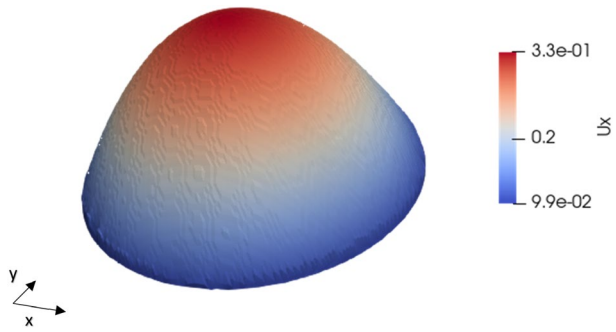

Fig. 21 Elevation of the numerical solution

The results of the convergence test can be seen in Fig. 20, whilst the elevation of the solution for the finest mesh can be seen in Fig. 21. From the figures, it is clear that the method converges optimally and remains well conditioned.

This example indicates that the method performs well for unfitted problems on curved domains, with essential boundary conditions.

Poisson problem on annulus domain with unfitted essential boundary

The final example considers the solution of the Poisson equation on an annulus, subject to unfitted essential boundary conditions:

$$\begin{aligned} -\Delta u &= 0, \\ u(a,\theta) &= \frac{a^2\cos(2\theta)}{2} + 1, \\ u(b,\theta) &= \frac{b^2\cos(2\theta)}{2} + 1 \end{aligned} \tag{26}$$

where $a = 0.72$, $b = 0.37$, the physical domain is defined $\Omega = (0.37, 0.72) \times (0, 2\pi)$ and the background mesh domain is $\Omega_m = (-1.05, 1.05) \times (-1.05, 1.05)$. The analytical solution is given by:

$$u(r,\theta) = \frac{r^2\cos(2\theta)}{2} + 1 \tag{27}$$

As with the previous example, it is noted that whilst this is a radial problem, the numerical solution was carried out using Cartesian coordinates. In addition, the circular boundary of the physical domain is approximated using piecewise linear segments within each element.

An example of one of the meshes used in the analysis that shows the boundaries marked with a black line, can be seen in Fig. 22.

The results of the convergence test can be seen in Fig. 23, whilst the elevation of the solution for the finest mesh can be seen in Fig. 24. From the figures, it is clear that the method converges optimally and remains well conditioned.

This example again indicates that the method performs well for unfitted problems on curved domains, with essential boundary conditions.

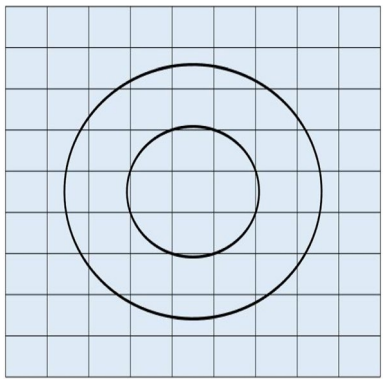

Fig. 22 Finite element mesh used in the analysis and unfitted boundaries

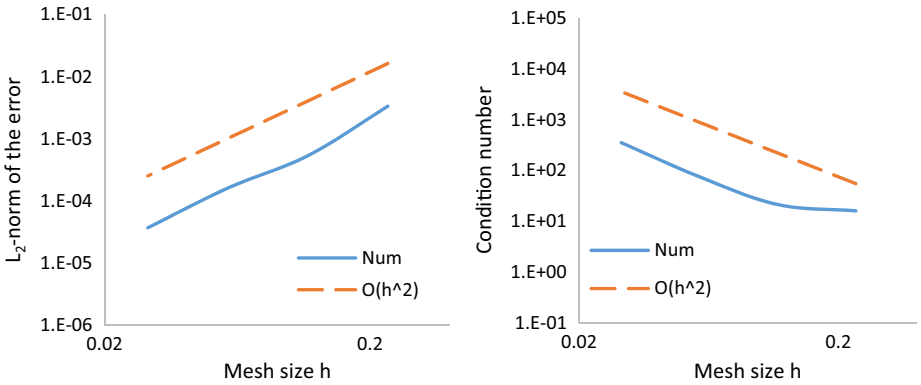

Fig. 23 Plot of the L_2-norm of the error and 2-norm condition number

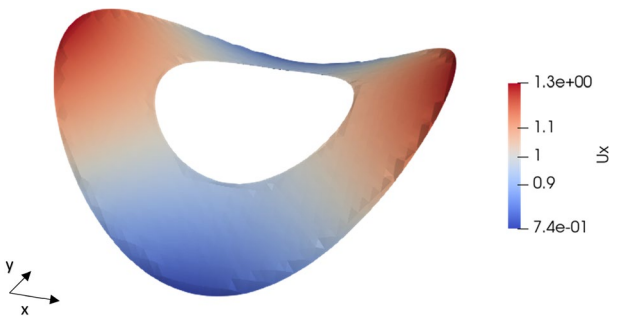

Fig. 24 Elevation of the numerical solution

Concluding remarks

A novel unfitted finite element method has been presented that allows for strong enforcement of boundary and interface conditions, as well as cut element stability. This is achieved through the use of multi-point constraints that have the additional benefits of avoiding the need for penalty parameters, and allowing the constrained degrees of freedom to be eliminated from the system of equations. This allows for the simulation of problems with both strong and weak discontinuities without introducing additional

degrees of freedom that could significantly improve computational efficiency. In addition to this, the method does not require special enrichment functions and can capture strong and weak discontinuities using only the standard finite element basis functions. The numerical examples presented have shown that the method converges optimally under mesh refinement and remains well conditioned. Whilst the present work focuses on the Poisson problem, the approach could be employed for range of other problems.

Acknowledgements
I would like to thank the Resilient Structures and Construction Materials (RESCOM) group at Cardiff University for their support throughout and in particular Tony Jefferson for the numerous inspiring, helpful discussions and advice.

Author contributions
The author read and approved the final mansucript.

Funding
Financial support from the UKRI-EPSRC Grant EP/P02081X/1 "Resilient Materials for Life (RM4L)" is gratefully acknowledged.

Availability of data and materials
Information on the data underpinning the results presented here, including how to access them, can be found in the Cardiff University data catalogue at (https://doi.org/10.17035/d.2022.0217821122).

Declarations

Competing interests
The author declares that they have no competing interests.

Received: 12 January 2022 Accepted: 20 August 2022
Published online: 21 September 2022

References

1. Strouboulis T, Babuška I, Copps K. The design and analysis of the generalized finite element method. Comput Methods Appl Mech Eng. 2000;181:43–69.
2. Strouboulis T, Copps K, Babuška I. The generalized finite element method. Comput Methods Appl Mech Eng. 2001;190:4081–193.
3. Strouboulis T, Copps K, Babuška I. The generalized finite element method: an example of its implementation and illustration of its performance. Int J Numer Meth Eng. 2000;47:1401–17.
4. Duarte CAM, Babuška I, Oden JT. Generalized finite element methods for three-dimensional structural mechanics problems. Comput Struct. 2000;77:215–32.
5. Gupta V, Kim DJ, Duarte CA. Analysis and improvements of global-local enrichments for the generalized finite element method. Comput Methods Appl Mech Eng. 2012;245–246:47–62.
6. O'Hara P, Duarte CA, Eason T. A two-scale generalized finite element method for interaction and coalescence of multiple crack surfaces. Eng Fract Mech. 2016;163:274–302.
7. Zhang Q. DOF-gathering stable generalized finite element methods for crack problems. Numer Methods Partial Differ Equ. 2020;36:1209–33.
8. Zhang Q, Cui C. Condensed generalized finite element method. Numer Methods Partial Differ Equ. 2021;37:1847–68.
9. Iqbal M, Alam K, Ahmad A, Maqsood S, Ullah H, Ullah B. An enriched finite element method for efficient solutions of transient heat diffusion problems with multiple heat sources. Eng Comput. 2022;38:3381–97.
10. Ma J, Duan Q, Tian R. A generalized finite element method without extra degrees of freedom for large deformation analysis of three-dimensional elastic and elastoplastic solids. Comput Methods Appl Mech Eng. 2022;392: 114639.
11. Zhang Q, Cui C, Banerjee U, Babuška I. A condensed generalized finite element method (CGFEM) for interface problems. Comput Methods Appl Mech Eng. 2022;391: 114527.
12. Belytschko T, Black T. Elastic crack growth in finite elements with minimal remeshing. Int J Numer Meth Eng. 1999;45:601–20.
13. Moës N, Dolbow J, Belytschko T. A finite element method for crack growth without remeshing. Int J Numer Meth Eng. 1999;46:131–50.
14. Fries TP, Belytschko T. The intrinsic xfem: a method for arbitrary discontinuities without additional unknowns. Int J Numer Meth Eng. 2006;68:1358–85.
15. Tian R, Wen L. Improved xfem—an extra-dof free, well-conditioning, and interpolating xfem. Comput Methods Appl Mech Eng. 2015;285:639–58.
16. Yu T, Bui TQ. Numerical simulation of 2-d weak and strong discontinuities by a novel approach based on XFEM with local mesh refinement. Comput Struct. 2018;196:112–33.
17. Bybordiani M, Latifaghili A, Soares D Jr, Godinho L, Dias-da-Costa D. An xfem multi-layered Heaviside enrichment for fracture propogation with reduced enhanced degrees of freedom. Int J Numer Meth Eng. 2021;122:3425–47.

18. Tian W, Huang J, Jiang Y, Chen R. A parallel scalable domain decomposition preconditioner for elastic crack simulation using XFEM. Int J Numer Meth Eng. 2022;123:3393–417.
19. Hansbo A, Hansbo P. An unfitted finite element method, based on Nitche's method, for elliptic interface problems. Comput Methods Appl Mech Eng. 2002;191:5537–52.
20. Hansbo A, Hansbo P. A finite element method for the simulation of strong and weak discontinuities in solid mechanics. Comput Methods Appl Mech Eng. 2004;193:3523–40.
21. Burman E, Claus S, Hansbo P, Larson MG, Massing A. CutFEM: discretizing geometry and partial differential equations. Int J Numer Meth Eng. 2015;104:472–501.
22. Claus S, Kerfriden P. A CutFEM method for two-phase flow problems. Comput Methods Appl Mech Eng. 2019;348:185–206.
23. Lozinski A. CutFEM without cutting the mesh cells: a new way to impose Dirichlet and Neumann boundary conditions on unfitted meshes. Comput Methods Appl Mech Eng. 2019;356:75–100.
24. Kerfriden P, Claus S, Mihai IC. A mixed-dimensional cutfem methodology for the simulation of fibre-reinforced composites. Adv Model Simul Eng Sci. 2020;7:18.
25. Mikaeili E, Claus S, Kerfriden P. Concurrent multiscale analysis without meshing: microscale representation with CutFEM and micro/macro model blending. Comput Methods Appl Mech Eng. 2022;393: 114807.
26. Melenk JM, Babuška I. The partition of unity finite element method: basic theory and applications. Comput Methods Appl Mech Eng. 1996;139:289–314.
27. Babuška I, Melenk JM. The partition of unity method. Int J Numer Meth Eng. 1997;40:727–58.
28. Song JH, Areias PMA, Belytschko T. A method for dynamic crack and shear band propagation with phantom nodes. Int J Numer Meth Eng. 2006;67:868–93.
29. Aragón AM, Simone A. The discontinuity-enriched finite element method. Int J Numer Meth Eng. 2017;112:1589–613.
30. van den Boom SJ, Zhang J, van Keulen F, Aragón AM. A stable interface-enriched formulation for immersed domains with strong enforcement of essential boundary conditions. Int J Numer Meth Eng. 2019;120:1163–83.
31. Soghrati S, Aragón AM, Duarte CA, Geubelle PH. An interface-enriched generalized fem for problems with discontinuous gradient fields. Int J Numer Meth Eng. 2012;89:991–1008.
32. Liu D, van den Boom SJ, Simone A, Aragón AM. An interface-enriched generalized finite element formulation for locking-free coupling of non-conforming discretizations and contact. Comput Mech. 2022. https://doi.org/10.1007/s00466-022-02159-w.
33. Oliver J, Huespe AE, Sanchez PJ. A comparative study on finite elements for capturing strong discontinuities: E-FEM vs X-FEM. Comput Methods Appl Mech Eng. 2006;195:4732–52.
34. Dias-da-Costa D, Alfaiate J, Sluys LJ, Areias P, Julio E. An embedded formulation with conforming finite elements to capture strong discontinuities. Int J Numer Meth Eng. 2013;93:224–44.
35. Nikolić M, Do XN, Ibrahimbegovic A, Nikolić Ž. Crack propagation in dynamics by embedded strong discontinuity approach: enhanced solid versus discrete lattice model. Comput Methods Appl Mech Eng. 2018;340:480–99.
36. Freeman BL, Bonilla-Villalba P, Mihai IC, Alnaas WF, Jefferson AD. A specialised finite element for simulating self-healing quasi-brittle materials. Adv Model Simul Eng Sci. 2020;7:32.
37. Liu F. Modeling hydraulic fracture propagation in permeable media with an embedded strong discontinuity approach. Int J Numer Anal Meth Geomech. 2020;44:1634–55.
38. Stanić A, Brank B, Ibrahimbegovic A, Matthies HG. Crack propagation simulation without crack tracking algorithm: embedded discontinuity formulation with incompatible modes. Comput Methods Appl Mech Eng. 2021;386: 114090.
39. Saksala T. Effect of inherent microcrack populations on rock tensile fracture behaviour: numerical study based on embedded discontinuity finite elements. Acta Geotech. 2022;17:2079–99.
40. Tian R. An extra-dof-free and linearly independent enrichments in GFEM. Comput Methods Appl Mech Eng. 2013;266:1–22.
41. Hou W, Jiang K, Zhu X, Shen Y, Li Y, Zhang X, Hu P. Extended isogeometric analysis with strong imposing essential boundary conditions for weak discontinuous problems using B++ splines. Comput Methods Appl Mech Eng. 2020;370: 113135.
42. Babuška I. The finite element method with penalty. Math Comp. 1973;27:221–8.
43. Hansbo P. Nitsche's method for interface problems in computational mechanics. GAMM-Mitteilungen. 2005;28:183–206.
44. Rüberg T, Cirak F, García Aznar JM. An unstructured immersed finite element method for nonlinear solid mechanics. Adv Model Simul Eng Sci. 2016;3:22.
45. Babuška I. The finite element method with lagrangian multipliers. Numerische Math. 1973;20:179–92.
46. Moës N, Béchet E, Tourbier M. Imposing Dirichlet boundary conditions in the extended finite element method. Int J Numer Meth Eng. 2006;67:1641–69.
47. Kumar AV, Padmanabhan S, Burla R. Implicit boundary method for finite element analysis using non-conforming mesh or grid. Int J Numer Meth Eng. 2008;74:1421–47.
48. Pande S, Papadopoulos P, Babuška I. A cut-cell finite element method for Poisson's equation on arbitrary planar domains. Comput Methods Appl Mech Eng. 2021;383: 113875.
49. Badia S, Verdugo F, Martín AF. The aggregated unfitted finite element method for elliptic problems. Comput Methods Appl Mech Eng. 2018;336:533–53.
50. Burman E, Cicuttin M, Delay G, Ern A. An unfitted hybrid high-order method with cell agglomeration for elliptic interface problems. SIAM J Sci Comput. 2021;43:A859–82.
51. Hansbo P, Larson MG, Zahedi S. A cut finite element method for a Stokes interface problem. Appl Numer Math. 2014;85:90–114.
52. Höllig K, Reif U, Wipper J. Weighted extended b-spline approximation of Dirichlet problems. SIAM J Numer Anal. 2001;39:442–62.

53 Main A, Scovazzi G. The shifted boundary method for embedded domain computations. Part 1: Poisson and Stokes problems. J Comput Phys. 2018;372:972–95.
54. Li K, Atallah NM, Main A, Scovazzi G. The shifted interface method: a flexible approach to embedded interface computations. Int J Numer Meth Eng. 2020;121:492–518.
55. Li K, Atallah NM, Rodriguez-Ferran A, Valiveti DM, Scovazzi G. The shifted fracture method. Int J Numer Meth Eng. 2021;122(6641–66791): 114527.

Publisher's Note